

Received November 26, 2019, accepted January 1, 2020, date of publication January 6, 2020, date of current version February 12, 2020.

Digital Object Identifier 10.1109/ACCESS.2020.2964525

# Radio Frequency Based Direction Sensing Using Massive MIMO

XIAOLU ZENG<sup>ID</sup><sup>1,2</sup>, FENG ZHANG<sup>ID</sup><sup>2,3</sup>, (Member, IEEE),  
BEIBEI WANG<sup>ID</sup><sup>2,3</sup>, (Senior Member, IEEE), AND  
K. J. RAY LIU<sup>ID</sup><sup>2,3</sup>, (Fellow, IEEE)

<sup>1</sup>National Laboratory of Radar Signal Processing, Xidian University, Xi'an 710071, China

<sup>2</sup>Department of Electrical and Computer Engineering, University of Maryland, College Park, MD 20742, USA

<sup>3</sup>Origin Wireless Inc., Greenbelt, MD 20770, USA

Corresponding author: Xiaolu Zeng (feiyi3709@sina.com)

This work was supported by the China Scholarship Council (CSC).

**ABSTRACT** Navigation systems have been widely used in modern applications in which the moving speed and direction estimations are two key steps. Instead of using traditional device-based orientation sensor such as accelerometer and magnetometer to estimate the moving direction, this paper presents a novel radio frequency (RF) signal-based moving direction sensing scheme by using 5G massive multiple input and output (MIMO) system. We first explore the energy distribution of the received signal in massive MIMO in both near- and far-field scenarios. The energy distribution in near-field is proved to be highly related to the geometric shape of the antenna deployment. In contrast, the energy distribution turns out to be a stationary sinc-like focusing beam in far-field scenario. Inspired by such an observation, we develop a novel method to estimate the speed of a moving target with respect to a single base station. The moving direction can be further determined by jointly considering the speed estimation results and the geometric property of the locations between the target and nearby base stations. Finally, numerical simulations show that the proposed RF-based method can achieve high accuracy in which the moving speed estimation error is less than 1.5m/s while the moving direction estimation error is within 2 degrees.

**INDEX TERMS** Massive MIMO, moving speed, moving direction, far-field, 5G.

## I. INTRODUCTION

Navigation systems have been widely used in modern applications, among which GPS is the most popular one. However, GPS cannot work well in non-line-of-sight (NLOS) situation [1] because of its requirement of an unobstructed line-of-sight (LOS) to four or more GPS satellites. As a result, inertial navigation system (INS) [2], [3] has been regarded as an effective supplement of GPS because it is a self-contained navigation technique. In an INS, moving speed and direction estimations are necessary to dead reckon the position of a moving object. As a result, how to estimate the moving speed and direction of a target has also been extensively studied.

Accelerometer, gyroscope and magnetometer are the three most commonly used sensors in an INS. In general, INS adopts certain data fusion methods [4] to jointly use the information extracted from different sensors to estimate the

The associate editor coordinating the review of this manuscript and approving it for publication was Lin Bai<sup>ID</sup>.

moving speed and direction of the target. They are accurate when the target is relatively stable. However, they suffer from the unavoidable mechanical resistance or magnetic interference, which causes accumulative errors from the truth, especially over a long time.

Vision/image based method aided by camera devices is another kind of popular ways to detect the moving speed and direction for metro vehicles. For example, the continuous image sequences of the road surface texture are analyzed to get the vehicle speed and direction estimations in [5]. To solve the high frame rate requirement, two parallel vehicle-borne devices are adopted to take the images simultaneously [6], [7]. Then, the vehicle speed and moving direction are extracted by image matching and parameter calibration schemes. Although those vision based methods can achieve good accuracy after rounds of improvement, their requirements of sufficient image resolution and computational power becomes a bottleneck in real-time applications.

RF-based methods such as direction-of-arrival (DOA) estimation has also been widely explored to estimate the direction of a target with respect to the antenna array [8], [9]. Recently, massive MIMO [10] is shown to further improve the DOA estimation accuracy because of its high degree of freedom and angular resolution. In addition, massive MIMO/access point (AP) generates a huge number of data which can be used by training-based approach for moving speed and direction estimation such as deep learning [11], K-means [12]. However, DOA-based methods usually estimate the incoming direction of the received signal rather than the moving direction of a target. Training-based approach requires plenty of data to train the parameters whenever the wireless propagation property changes, thus hindering practical usability.

Different from most existing works which rely on dedicated devices, this paper is inspired by the principle of time reversal (TR), based on which many powerful indoor target localization and tracking methods have been developed [13]–[18]. In particular, the time-reversal resonating strength (TRRS) [14] is proved to be a stationary and location-independent focusing-ball shaped distribution around the receiver [17]. By leveraging such an observation, a target tracking method with centimeter-level accuracy has been proposed and verified by extensive experiments [18].

Intuitively, the afore-mentioned indoor localization systems [17], [18] take advantage of the massive multipath components existing in the indoors and establish a link between the statistical property of the received signal and the moving speed of the target. However, when it comes to outdoor scenario with cellular communication being widely deployed, there are two new challenges. First, it has been shown through extensive measurements [19]–[21] that there are much less multipaths in an outdoor environment (e.g., a street or plaza) than in indoors. In addition, the 5G cellular network will become ultra dense (about 40 – 50 BSs/km<sup>2</sup>) so as to provide seamless coverage [22]. In this case, the received signal is more likely to consist of both LOS and NLOS signal components while the NLOS signal dominates in an indoor area. Second, multipath signals in indoors [17] are assumed to impinge from all directions around the receiver symmetrically. As a result, the TRRS energy distribution of the received signal is shown to be a symmetric Bessel-like focusing ball around the receiver, which cannot provide the direction information. Is there a good alternative that not only exhibits a similar focusing effect but also provides direction information?

In this paper, we address the two aforementioned problems on the base of 5G massive MIMO communication scheme and propose a simple yet practical device-free moving speed and direction estimation method. Specifically, a massive MIMO system utilizes multiple antennas to physically generate a large number of signal components which play similar roles as multipaths in a rich-scattering environment. In addition, the incident signals generated by massive MIMO can only get to the receiver from the transmitter side. We then prove that in far-field scenario, the autocorrelation function

strength (ACFS) distribution of the received signal around the receiver exhibits a sinc-like beam in spatial domain, which can provide direction information. By further using the dense deployment of 5G massive MIMO base stations (BSs) [22]–[24], a new radio frequency (RF) signal based moving speed and direction estimation method is proposed. In addition, it leverages the natural superposition property of the received signal, which reduces the computational load greatly. The main contributions of this work can be summarized as follows:

- We derive the ACFS distribution of the received signal of a massive MIMO communication system in both near- and far-field scenarios. In near-field situation, the ACFS distribution is closely related to the geometric parameters of the antenna array while it shows a stationary sinc-like beam in far-field scenario.
- Considering the practical far-field scenario, we develop a moving speed estimation algorithm by using the aforementioned ACFS distribution, which achieves high accuracy with the speed estimation error less than 1.5m/s. Because the ACFS distribution of the received signal is stable, meaning the computation complexity for calculating the ACFS is linearly proportional to the received data size, the proposed speed estimation algorithm also enjoys a low complexity.
- Based on the speed estimation, we propose an approach to estimate the moving direction by further using the BS deployment information. Numerical simulations show that our method is environment independent and the moving direction estimation error is less than 2 degrees, which outperforms the benchmark methods i.e., DOA estimation methods [25]–[28], SenSpeed [29], GPS method [30], INS based methods [2], [3], massive MIMO based methods [9], [12], [31] and vision based methods [5], [6] in terms of accuracy and complexity.

The rest of the paper is organized as follows. In Section II, we introduce the signal model for a massive MIMO system and derive the ACFS distribution of the received signal in both near- and far-field scenarios respectively. Speed estimation and corresponding moving direction estimation methods are elaborated in Section IV. Extensive numerical simulations in Section V show the validity of the proposed approach. And Section VI concludes the paper.

## II. ACFS DISTRIBUTION OF MASSIVE MIMO

### A. SIGNAL MODEL

We assume a massive MIMO BS and a receiver fixed on a moving object. In Fig. 1, the BS denoted by ‘B’ is equipped with  $M$  antennas which communicate with the receiver simultaneously.  $H_B$  denotes the height difference between the BS and the receiver  $\mathbf{r}$ . Different from the typical Rician fading model, the LOS signal  $y_L(t)$  here is not a single component but the superposition of multiple signals transmitted by the massive antennas on the BS. Then, the complex form of the

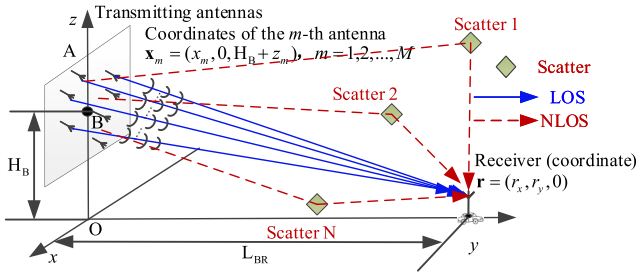


**FIGURE 1.** The set-up for a base station with massive MIMO(A: transmitting antennas, B: base station, r: receiver,  $H_B$ : height difference between the BS and the receiver  $r$ ).

received signal at base band can be expressed as [32], [33]

$$\begin{aligned} y(t) &= y_L(t) + y_N(t) + n(t), \\ y_L(t) &= \sqrt{K_L} \sum_{m=1}^M \frac{\exp(j(k|\mathbf{x}_m \mathbf{r}_t| + \phi_m))}{4\pi |\mathbf{x}_m \mathbf{r}_t|}, \\ y_N(t) &= \sqrt{K_N} \sum_{n=1}^N \exp[j(\omega_d t \cos \alpha_n + \phi_n)], \end{aligned} \quad (1)$$

where  $y_N(t)$  is the superposition of the NLOS signal components reflected from the surrounding scatterers.  $K_L$  and  $K_N$  are the power coefficients.  $k = 2\pi/\lambda$  denotes the wave number while  $\lambda$  is the wavelength.  $\omega_d$  is the Doppler frequency.  $\mathbf{x}_m$  denotes the coordinate of the  $m$ -th antenna and  $\mathbf{r}_t$  is the coordinate of the receiver location at time  $t$ .  $|\mathbf{x}_m \mathbf{r}_t|$  denotes the spatial distance between  $\mathbf{x}_m$  and  $\mathbf{r}_t$ .  $n(t)$  is the complex additive white Gaussian noise (AWGN).  $\phi_m$  ( $m = 1, 2, \dots, M$ ) is the compound phase distortion of the  $m$ -th LOS path signal.  $\alpha_n$  and  $\phi_n$  are the DOA and phase distortion of the  $n$ -th NLOS path signal. In general,  $\phi_m$ ,  $\alpha_n$  and  $\phi_n$  ( $n = 1, 2, \dots, N$ ) can be assumed as i.i.d uniform distributions over  $[-\pi, \pi]$  [33], where  $N$  is the total number of NLOS signal components. In typical urban areas,  $N$  varies from tens to hundreds [19]–[21]. As a result, we set  $N$  as a random integer within  $10 \sim 100$  in this paper.

### B. ACF DISTRIBUTION OF THE NLOS SIGNAL

Recalling (1), the ACF of the received signal at two different time stamps  $t_0$  and  $t_s$  is given by

$$\eta_y = \mathbb{E}_{\alpha, \phi}[y(t_0)y^*(t_s)] \quad (2)$$

$$= \mathbb{E}_{\phi}[y_L(t_0)y_L^*(t_s)] + \mathbb{E}_{\alpha, \phi}[y_N(t_0)y_N^*(t_s)]. \quad (3)$$

where  $\mathbb{E}$  represents the expectation w.r.t.  $\alpha$  and  $\phi$ . Note that in (1), we only know the distributions of  $\phi_m$ ,  $\alpha_n$  and  $\phi_n$ . Hence, we should take the expectations over variables  $\alpha$  and  $\phi$  to get the ACF of the received signal in (2) and (3). In addition,  $y_L(t)$  is not related to  $\alpha$ . Hence, we omit  $\alpha$  when we compute the ACF of  $y_L(t)$ . This notation is commonly used by researchers in this area. Interested readers can refer to [33] and the references therein for details. Moreover, ACFS is defined as  $|\eta_y|^2$ . The cross-correlation terms between  $y_L(t)$ ,  $y_N(t)$  and  $n(t)$  are zeros because they are independent terms

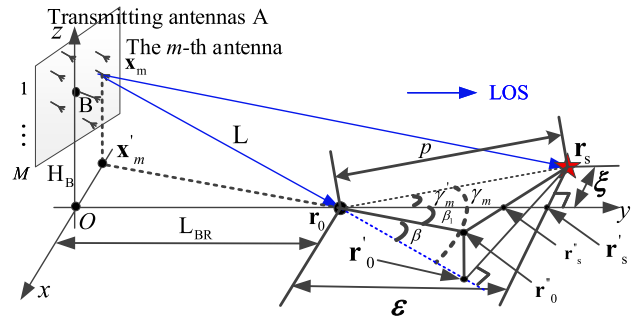


**FIGURE 2.** Signal propagation geometry between two different locations  $\mathbf{r}_0$  and  $\mathbf{r}_s$  of the target.

with zero mean. In addition, we omit term  $\mathbb{E}[n(t_0)n^*(t_s)] = \sigma^2$ , which is a constant. From [17], [33], ACF of the NLOS signal is given by

$$\eta_{yN} = \eta_{yN}(\mathbf{r}_0, \mathbf{r}_s) = \mathbb{E}_{\alpha, \phi}[y_N(t_0)y_N^*(t_s)] = K_N J_0(kp). \quad (4)$$

where  $J_0$  is the 0-order Bessel function. Hereafter, as shown in Fig. 2,  $\mathbf{r}_0$  and  $\mathbf{r}_s$  denote the two nearby positions of the moving object at two different time stamps  $t_0$  and  $t_s$  on the ground ( $xOy$  plane).  $p = |\mathbf{r}_0 \mathbf{r}_s|$ ,  $\epsilon$  and  $\xi$  represent the Euclidean spatial distance, range and cross-range between  $\mathbf{r}_0$  and  $\mathbf{r}_s$ , respectively. In addition, we define the following angle related notations shown in Fig. 2, i.e.,  $\angle \mathbf{r}_s \mathbf{r}_0 \mathbf{r}'_s = \gamma'_m$ ,  $\angle \mathbf{r}_s \mathbf{r}_0 \mathbf{r}_0'' = \gamma_m$ ,  $\angle \mathbf{r}'_s \mathbf{r}_0 \mathbf{r}_0'' = \beta_1$ ,  $\angle \mathbf{r}_0'' \mathbf{r}_0 \mathbf{r}'_0 = \beta$ , where  $\mathbf{r}'_0$  lies in the extension line of  $\mathbf{l}_{\mathbf{x}_m \mathbf{r}_0}$  satisfying that  $\mathbf{l}_{\mathbf{x}_m \mathbf{r}'_0} \perp \mathbf{l}_{\mathbf{r}_s \mathbf{r}'_0}$ . And  $\mathbf{r}_0''$  is the projection of  $\mathbf{r}'_0$  on the  $xOy$  plane. By using the geometrical relationships shown in Fig. 2, we can achieve

$$\begin{aligned} \cos \gamma_m &= \cos \beta \cdot \cos(\beta_1 + \gamma'_m), \quad \cos \gamma'_m = \epsilon/p, \\ \cos \beta &= \frac{\sqrt{L_{BR}^2 + x_m^2}}{\sqrt{L_{BR}^2 + (H_B + z_m)^2 + x_m^2}}, \\ \cos \beta_1 &= \frac{L_{BR}}{\sqrt{L_{BR}^2 + x_m^2}}. \end{aligned} \quad (5)$$

### III. ACFS DISTRIBUTION OF MASSIVE MIMO

#### A. ACFS DISTRIBUTION OF THE LOS SIGNAL

From (1), the ACF distribution of the LOS signal  $y_L(t)$  is

$$\begin{aligned} \eta_{yL} &= \mathbb{E}_{\phi}[y_L(t_0)y_L^*(t_s)] = K_L \\ &\times \sum_{i=1}^M \sum_{m=1}^M \mathbb{E}_{\phi} \left\{ \frac{\exp[jk(|\mathbf{x}_i \mathbf{r}_0| - |\mathbf{x}_m \mathbf{r}_s|) + j(\phi_i - \phi_m)]}{(4\pi)^2 |\mathbf{x}_i \mathbf{r}_0| |\mathbf{x}_m \mathbf{r}_s|} \right\}. \end{aligned} \quad (6)$$

In practice,  $||\mathbf{x}_i \mathbf{r}_0| - |\mathbf{x}_m \mathbf{r}_s||$  which represents the path difference is within meters.  $|\mathbf{x}_i \mathbf{r}_0|$  and  $|\mathbf{x}_m \mathbf{r}_s|$  denote the distance between the antenna and target, which vary from several meters to hundreds meters. Next, we separate the derivation of (6) into near- and far-field cases.

### 1) NEAR-FIELD SCENARIO

To compute (6), when  $i = m$ , we have

$$\eta_{y_L}^{N_{1st}} = K_L \sum_{m=1}^M \mathbb{E}_\phi \{ \exp[jk(|\mathbf{x}_m \mathbf{r}_0| - |\mathbf{x}_m \mathbf{r}_s|)] \}. \quad (7)$$

$$|\mathbf{x}_m \mathbf{r}_s| = \sqrt{|\mathbf{x}_m \mathbf{r}_0|^2 + p^2 - 2|\mathbf{x}_m \mathbf{r}_0|p \cos \gamma_m}. \quad (8)$$

When  $i \neq m$  in (6), i.e.,

$$\eta_{y_L}^{N_{2nd}} = K_L \sum_{i=1}^M \sum_{m=1, m \neq i}^M \mathbb{E}_\phi \{ \exp[j(\Psi_{im} + \Phi)] \}, \quad (9)$$

where  $\Psi_{im} = k|\mathbf{x}_i \mathbf{r}_0| - k|\mathbf{x}_m \mathbf{r}_s|$  and  $\Phi = \phi_i - \phi_m$ . Then, the ACFS can be expressed as  $|\eta_y^N|^2 = |\eta_{y_L}^{N_{1st}} + \eta_{y_L}^{N_{2nd}} + \eta_{y_N}|^2$ .

In the near-field scenario,  $H_B, z_m, x_m$  are within several meters while  $L_{BR} \leq 10H_B \leq 50m$ . Therefore,  $\cos \gamma_m$  in (5) is in a complicated form, which results in that there is no close form of  $\eta_{y_L}^{N_{1st}}, \eta_{y_L}^{N_{2nd}}$  and the ACFS  $|\eta_y^N|^2$ . In this case, Fig. 4 numerically shows the ACFS distributions of a uniform linear array (ULA) and a uniform circular array (UCA). More discussions are given in Section III-B.

### 2) FAR-FIELD SCENARIO

In practice, far-field situation (i.e.,  $L_{BR} \geq 10H_B \geq 50m$ ) is more popular for outdoor targets because the future 5G cellular network will become ultra-dense with a density of  $40 - 50$  BSs/km<sup>2</sup> [22]. Even though  $L_{BR} \leq 50m$  for some BSs,  $L_{BR} \geq 50m$  can be true for some other nearby BSs at the same time. Therefore, far-field condition can be easily satisfied in the 5G cellular network system. In this case,  $|\mathbf{x}_m \mathbf{r}_s| \geq L_{BR} \gg H_B, \mathbf{x}_m, \mathbf{z}_m$  and  $p = |\mathbf{r}_0 \mathbf{r}_s|$ . Moreover,  $|\mathbf{x}_i \mathbf{r}_0|$  and  $|\mathbf{x}_m \mathbf{r}_s|$  in the denominator of (6) are just amplitude scalers which can be approximated as the same constant. As a result, we will omit the denominator of (6) in the following.

In (6), when  $i = m$ , in  $\Delta \mathbf{x}_m \mathbf{r}_0 \mathbf{r}_s$ , we have

$$|\mathbf{x}_m \mathbf{r}_s|^2 = (|\mathbf{x}_m \mathbf{r}_0| - p \cos \gamma_m)^2 + p \sin \gamma_m^2 \approx (|\mathbf{x}_m \mathbf{r}_0| - p \cos \gamma_m)^2. \quad (10)$$

$$\begin{aligned} | |\mathbf{x}_m \mathbf{r}_0| - |\mathbf{x}_m \mathbf{r}_s| | &\approx p \cos \gamma_m = \frac{-L\epsilon + x_m \xi}{\sqrt{L^2 + x_m^2}} \\ &\approx -\epsilon + x_m \xi / L, \\ L &= \sqrt{L_{BR}^2 + (H_B + z_m)^2 + x_m^2} \end{aligned} \quad (11)$$

where  $L$  is the distance between the antenna and target. Substituting (11) into (7), We get

$$\eta_{y_L}^{F_{1st}} = \frac{K_L A_e \exp(jk\epsilon)}{d} \text{sinc}\left(\frac{k\xi A_e}{2L}\right), \quad (12)$$

where  $\text{sinc}(t) = \sin(t)/t$ ,  $A_e = Md$  while  $d = \lambda$  is the inner element space.

When  $i \neq m$ , similar to (10) and (11), we can get that

$$| |\mathbf{x}_i \mathbf{r}_0| - |\mathbf{x}_m \mathbf{r}_s| | = -\epsilon + [x_m(\xi - \Delta \mathbf{x}_{im})/L], \quad (13)$$

where  $\Delta \mathbf{x}_{im} = |(i-m)d|$ . Next, we discuss  $\Phi = (\phi_i - \phi_m)$  in (9). Different from [33], we consider a more general case in

which  $\phi_i$  and  $\phi_m$  are uniformly distributed over  $[\Phi_{min}, \Phi_{max}]$ . The probability density function (PDF) of  $\Phi$  is

$$f_\Phi(\phi) = \begin{cases} \phi_R + \phi, & -\phi_R \leq \phi \leq 0, \\ \phi_R - \phi, & 0 \leq \phi \leq \phi_R. \end{cases} \quad (14)$$

where  $\phi_R = \Phi_{max} - \Phi_{min}$ . Then, (9) is given by

$$\begin{aligned} \eta_{y_L}^{F_{2nd}}(i, m) &= \exp(j\Psi_{im}) \int_{-\phi_R}^{\phi_R} f_\Phi(\phi) \exp(j\phi) d\phi. \\ &= 2 \exp(j\Psi_{im})(1 - \cos(\phi_R)). \end{aligned} \quad (15)$$

In general, it is assumed that  $\Phi_{min} = -\pi$  and  $\Phi_{max} = \pi$  [33]. Therefore,  $\phi_R = 2\pi$  and  $\eta_{y_L}^{F_{2nd}}(i, m) = 0$ . Consequently,  $\eta_{y_L}^{F_{2nd}} = \sum_{i=1}^M \sum_{m=1, m \neq i}^M \eta_{y_L}^{F_{2nd}}(i, m) = 0$ . Then,

$$\eta_{y_L}^F = \eta_{y_L}^{F_{1st}} + \eta_{y_L}^{F_{2nd}} = \frac{K_L A_e \exp(jk\epsilon)}{d} \text{sinc}\left(\frac{k\xi A_e}{2L}\right). \quad (16)$$

In a more general case where  $\Phi_{min} \neq -\pi$  and  $\Phi_{max} \neq \pi$ ,  $\eta_{y_L}^{F_{2nd}}(i, m)$  in (15) does not always equal to 0. Since in (15) that  $1 - \cos(\phi_R)$  is a constant once  $\phi_R$  is determined, we focus on the  $\exp(j\Psi_{im})$  in the following by dividing (13) into  $-\epsilon$ ,  $\frac{x_m \xi}{L}$  and  $\frac{x_m \Delta \mathbf{x}_{im}}{L}$ . Next, we define

$$\vec{\Psi}_{im} = x_m \Delta \mathbf{x}_{im}/L = md|(i-m)|d/L, \quad (17)$$

$$\eta_{y_L}^{F_{2nd}}(m) = K_L \sum_{\substack{i=1, \\ i \neq m}}^M \exp(jk\vec{\Psi}_{im}) \approx K_L \sum_{i=1}^{M-1} \exp(jk\delta). \quad (18)$$

where  $\delta$  is a small factor to approximate  $\vec{\Psi}_{im}$  because  $m|(i-m)|d^2 \ll L$  holds in far-field scenario. Extra error may be induced by this approximation. However, simulations in Fig. 5 show that it is tolerable. Jointly using (13) and (18) and considering all the  $(i, m)$  pairs, we can get that

$$\begin{aligned} \eta_{y_L}^{F_{2nd}} &= MK_L \sum_{i=1}^M \exp[jk(\epsilon + x_m(\xi - \delta)/L)] \\ &= MK_L (1 - \cos(\phi_R)) \frac{A_e \exp(jk\epsilon)}{d} \text{sinc}\left(\frac{k(\xi - \delta)A_e}{2L}\right). \end{aligned} \quad (19)$$

As a result,

$$\eta_{y_L}^F = \eta_{y_L}^{F_{1st}} + \eta_{y_L}^{F_{2nd}} = K_L \text{sinc}\left(\frac{k(\xi - \delta_y)A_e}{2L}\right) \quad (20)$$

$$\tan\left(\frac{kA_e \delta_y}{2L}\right) = \frac{(1 - \cos \phi_R) \sin \phi_y}{1 + (1 - \cos \phi_R) \cos \phi_y}, \quad \phi_y = \frac{kA_e \delta}{2L}. \quad (21)$$

The entire normalized ACFS is then given by

$$|\eta_y^F|^2 = |\eta_{y_L}^F + \eta_{y_N}|^2, \quad \text{with } \eta_{y_N} = K_N J_0(kp). \quad (22)$$

Evidently,  $\eta_{y_N}$  decays much faster than  $\eta_{y_L}^F$ . Moreover, extensive measurements [19], [21] show that usually  $K_L \geq K_N$  holds in a typical urban area. As a result, the ACFS is dominated by the  $\eta_{y_L}^F$ , i.e.,  $|\eta_y^F|^2 \approx |\eta_{y_L}^F|^2$ , which is verified by Fig. 3 and other the simulations in Section III-B.

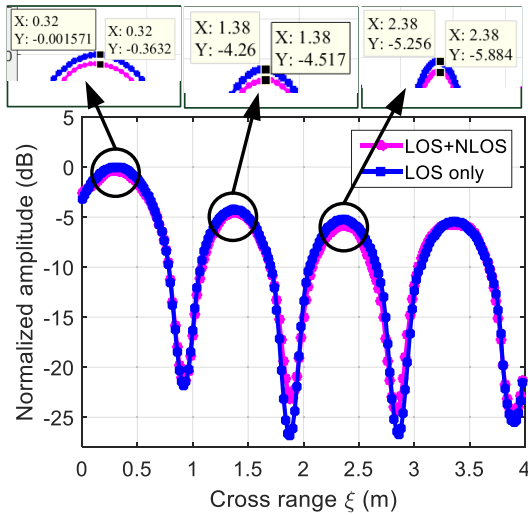


**FIGURE 3.** ACFS distribution with LOS and NLOS.

### B. VERIFICATION OF ACFS DISTRIBUTION

Assuming  $M = 100$ ,  $N = 50$ ,  $f_0 = 28\text{GHz}$  [34],  $d = \lambda$ ,  $H_B = 10\text{m}$ ,  $L_{BR} = 100\text{m}$  and  $K_L = K_N$ , Fig. 3 shows the ACFS numerically computed by (2) and (6). It is easy to conclude that the NLOS signal has little impact on the ACFS which is consistent with our analysis in (22). Fig. 4 shows the ACFS computed by (2) using the similar parameters with

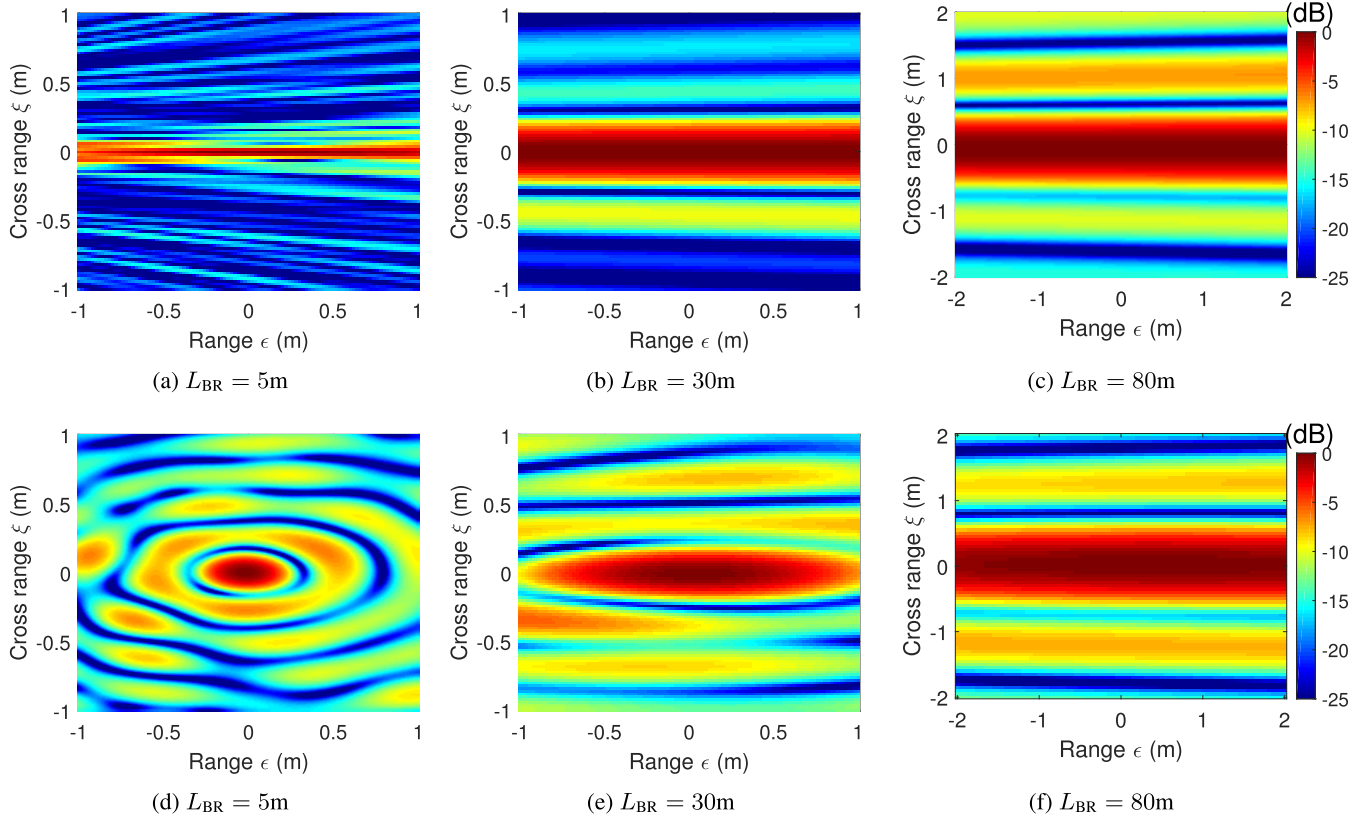


**FIGURE 4.** ACFS around the center, (a)-(c) ULA, (d)-(f) UCA.

Fig. 3 but different  $L_{BR}$ . When  $L_{BR} \leq 50\text{m}$ , ULA and UCA show different ACFS distributions while a similar beam pattern when  $L_{BR} \geq 50\text{m}$ , which also matches our derivation in (22).

From (20) and (22), the ACFS distribution is only related to  $\xi$  given a fixed  $L$ . Hence, we set  $\epsilon = 0$  and study the ACFS distribution versus different  $\xi$ . As shown in Fig. 5, the pattern of these two matches well while there is a little bias because of the approximation  $\delta$  in (18) especially when  $\xi \leq 1\text{m}$ . However, the following angle estimation method is based on the peak distance between the second and third peak. In Fig. 5, the aforementioned peak distances obtained by (2) and (20) are consistent. As a result, the bias and mismatch of the two when  $\xi \leq 1\text{m}$  does not influence our angle estimation.

### IV. MOVING SPEED AND DIRECTION ESTIMATION METHOD

We first define range and cross-range direction in Fig. 6(a). The peak distance  $p$  and moving time  $t$  are depicted in Fig. 6(b). Then, we introduce a new target speed estimation method and further a novel moving direction estimation approach.

#### A. SPEED ESTIMATION

From (22), the ACFS measured at the receiver is just a sampled version of  $\left| \text{sinc}\left(\frac{k(\xi - \delta_y)A_e}{2L}\right) \right|^2$  as depicted in Fig. 5.

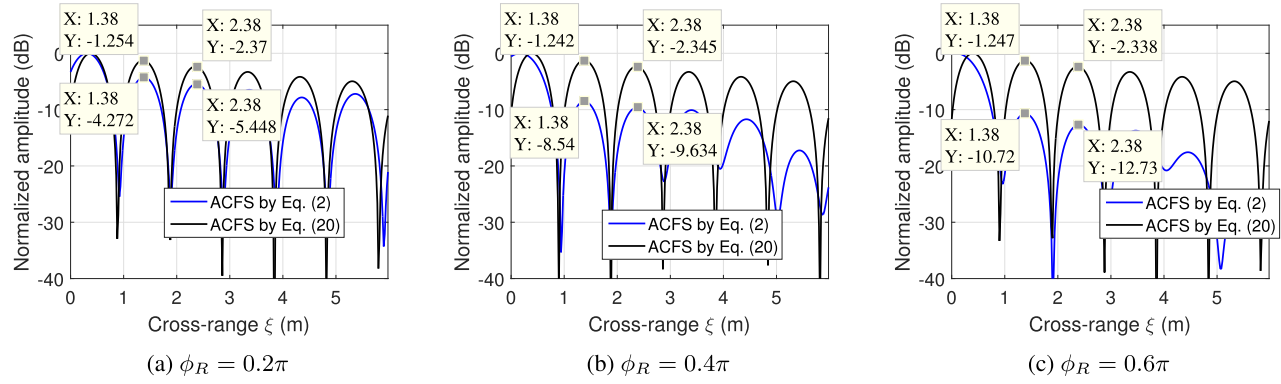


FIGURE 5. ACFS distribution from equation (2) and (20).

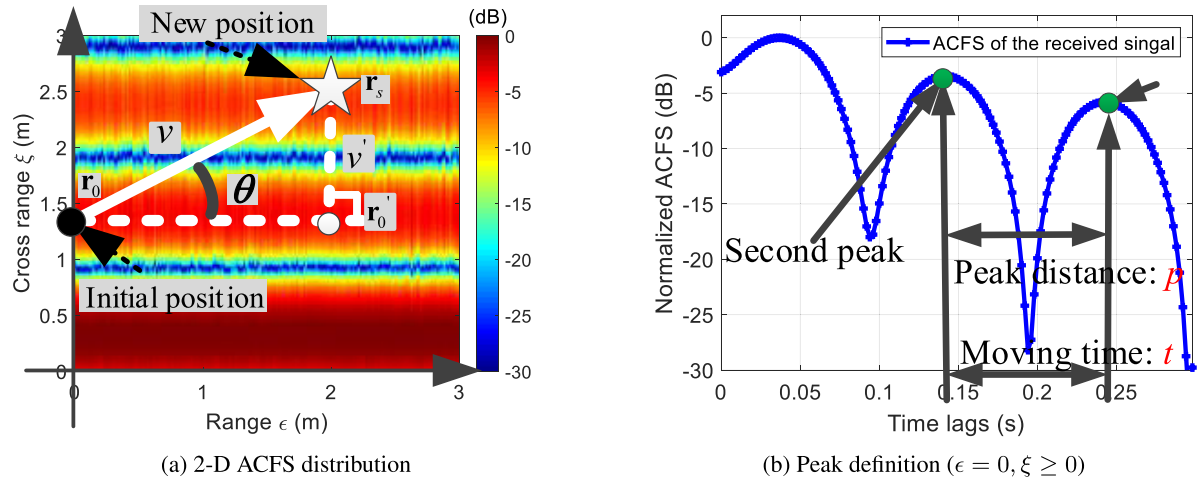
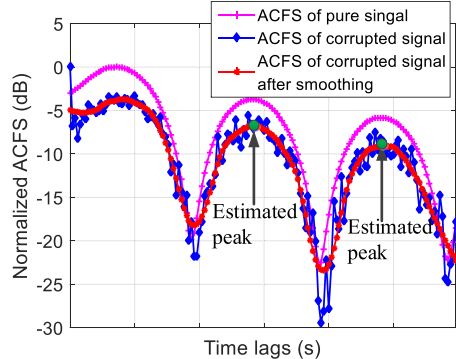
FIGURE 6. ACFS around an intended center ( $\epsilon = 0, \xi = 0$ ).

FIGURE 7. Curve smoothing.

As a result, we can compute the peak distance  $p = 2.034L/kA_e \approx 1.017\text{m}$  which matches with our simulation ( $p = 1\text{m}$ ) in Fig. 5. The moving time  $\hat{t}$  can be estimated by looking for the second and third peaks of the ACFS distribution curve. Then, the target speed is given by  $v = p/\hat{t}$ . Note that a local regression [35] method is applied first to smooth the ACFS curve to get rid of glitches caused by noise and other interference as shown in Fig. 7.

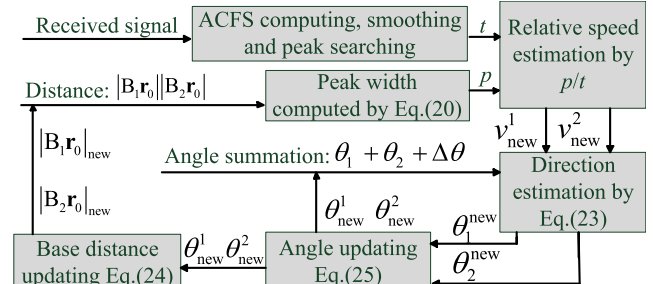
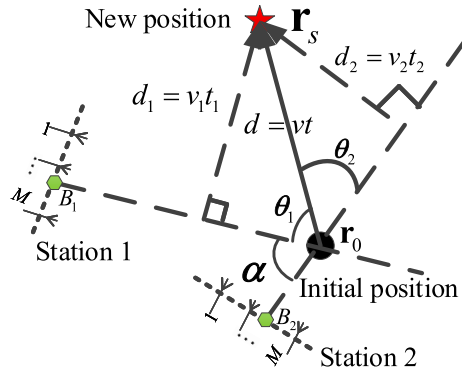
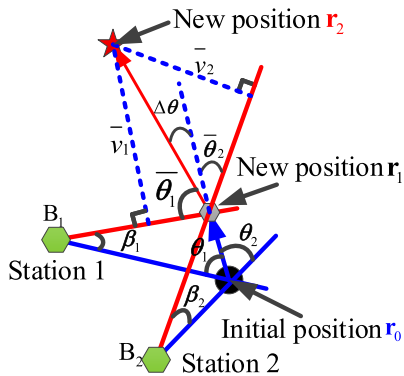


FIGURE 8. Key steps of the proposed method.

## B. DIRECTION ESTIMATION

Assuming that a target moves along  $\overrightarrow{\mathbf{r}_0\mathbf{r}_s}$  in Fig. 6(a), our speed estimation is actually  $v'$  rather than  $v$  because that the peak distance defined in Fig. 6(b) is along the cross-range direction  $(\overrightarrow{\mathbf{r}'_0\mathbf{r}_s})$ . However, by further using the geometry relationships between the two nearby BSs and target shown in Fig. 9, the true speed  $v$  can be expressed as

$$v = v_1/\sin\theta_1 = v_2/\sin\theta_2, \quad 180^\circ - \alpha = \theta_1 + \theta_2. \quad (23)$$

**FIGURE 9.** Direction estimation.**FIGURE 10.** Direction updating.

Since  $v_1$  and  $v_2$  are already estimated by our previous speed estimation method, we can obtain  $\theta_1$  and  $\theta_2$  by solving the two equations in (23). Next, we discuss how to update the estimation of  $\theta_1$  and  $\theta_2$  when the target keeps moving.

### C. DIRECTION ESTIMATION UPDATING

Fig. 10 shows three consecutive adjacent points  $\mathbf{r}_0$ ,  $\mathbf{r}_1$  and  $\mathbf{r}_2$  along the moving trace.  $\mathbf{r}_0$  is the initial point and  $\Delta\theta$  is the turning angle. From (23), we can obtain the estimation of  $\theta_1$ ,  $\theta_2$  and the true speed  $v$ . Thus, we have  $|\mathbf{r}_0\mathbf{r}_1| = vt$  and the distance between the target and BS

$$|\mathbf{B}_1\mathbf{r}_1| = \sqrt{|\mathbf{B}_1\mathbf{r}_0|^2 + |\mathbf{r}_0\mathbf{r}_1|^2 - 2|\mathbf{B}_1\mathbf{r}_0||\mathbf{r}_0\mathbf{r}_1|\cos\theta_1}. \quad (24)$$

Once we get the new  $|\mathbf{B}_1\mathbf{r}_1|$ , we update the ACFS distribution to estimate a new pair of  $(\bar{v}_1, \bar{v}_2)$ . By using triangular relationships, we can also easily get  $\beta_1$ ,  $\beta_2$  and

$$\begin{cases} \bar{\theta}_1 + \Delta\theta = \theta_1 + \beta_1 \\ \bar{\theta}_2 = \theta_2 - \beta_2 \end{cases} \Rightarrow \bar{\theta}_1 + \bar{\theta}_2 + \Delta\theta \text{ is obtained.} \quad (25)$$

Then, we can update (23). Finally, we use  $(\bar{v}_1, \bar{v}_2)$  and  $\bar{\theta}_1 + \bar{\theta}_2 + \Delta\theta$  to estimate  $\bar{\theta}_1$  and  $\bar{\theta}_2$  respectively. To have a high-level understanding, the flowchart of the proposed method is summarized in Fig. 8.

## V. SIMULATION RESULTS

In this section, we simulate a 5G communication system to evaluate the proposed method. In all the experiments, we set  $M = 100$ ,  $N$  as a random integer within  $10 \sim 100$ ,

$f_0 = 28\text{GHz}$  [34],  $d = \lambda$ ,  $H_B = 10\text{m}$ ,  $L_{BR} \geq 50\text{m}$ , SNR = 10dB and sampling rate  $f_s = 500\text{Hz}$ , if not otherwise indicated. In the following, we study the performance of the proposed system in six perspectives: 1) speed and direction estimation results; 2) impact of antenna number, 3) impact of the sample rate, 4) impact of SNR, 5) impact of antenna array configuration and 6) comparison with existing works.

### A. SPEED AND ANGLE ESTIMATION RESULTS

We first construct a practical case in which the target starts moving with a low speed of 5m/s, accelerates for 2 seconds, keeps constant speed for 1 second and finally decelerates. Fig. 11 shows that our method can achieve less than 1.5m/s speed estimation error. The direction estimation suffers from a relative large error at the beginning when  $(\theta_1 + \theta_2)$  is very close to  $90^\circ$ . Obviously, from (23),  $\sin(\theta_1 + \theta_2)$  changes smoothly when  $(\theta_1 + \theta_2)$  approaches to  $90^\circ$ . In other words, if there are errors in our previous  $v_1$  and  $v_2$  estimations,  $\sin(\theta_1 + \theta_2)$  just deviates a little. However, when  $(\theta_1 + \theta_2)$  is far away from  $90^\circ$ , our method becomes more accurate as shown in Fig. 11(c). Fig. 12 shows the empirical cumulative distribution function (CDF) of our method obtained from 1000 Monte Carlo trials for five different speeds. Overall, the 80 percentile of speed estimation error is within 1.0m/s while the direction estimation error is less than  $1.3^\circ$ .

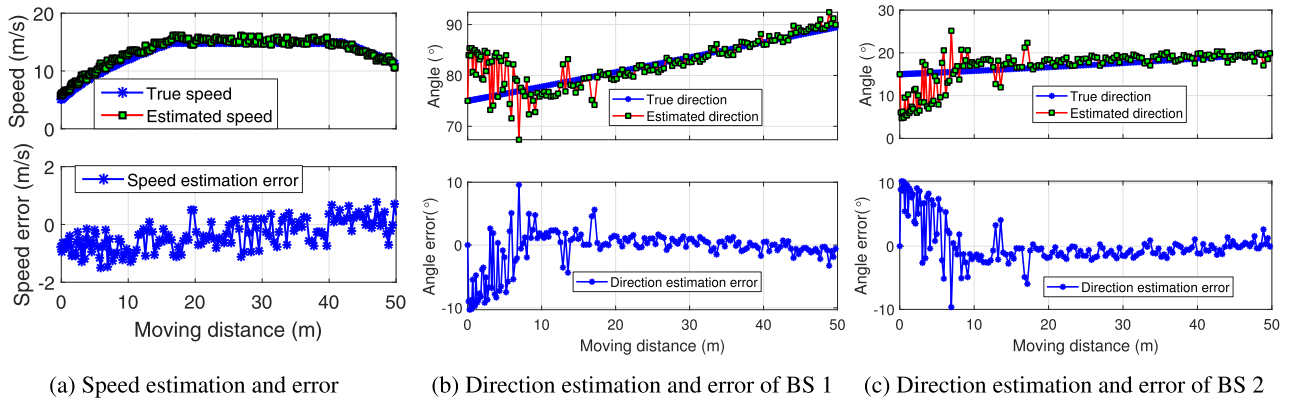
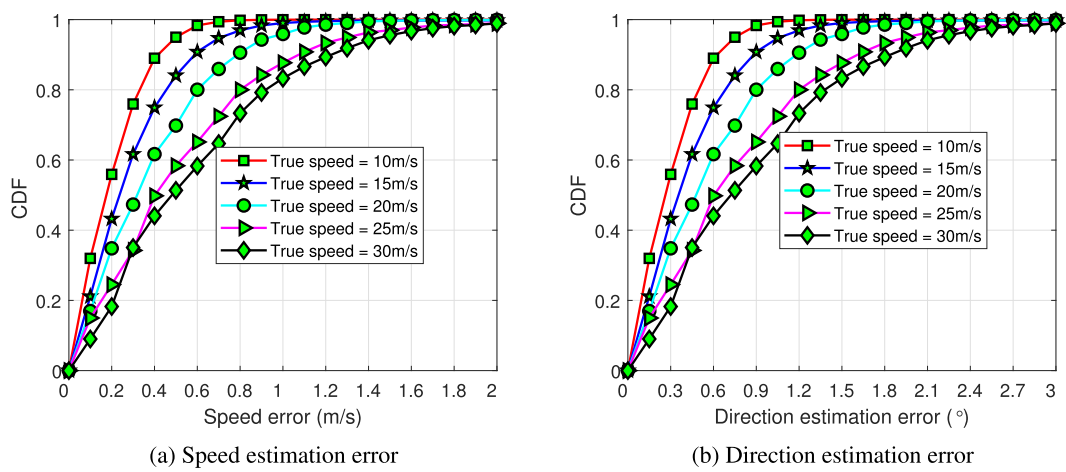
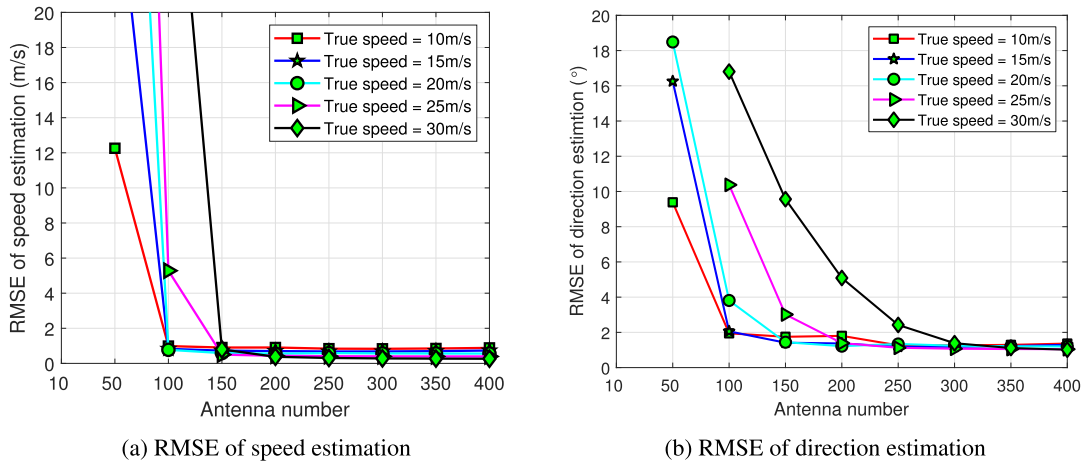
Note that ‘moving distance’ along x-axis means how far the target moves away from the starting point. Here, we only show the results when the moving distance is within 60m. However, situations with larger moving distances are also explored. While we omit corresponding plots, the direction estimation error accumulates at a moderate rate as the object moves too far away from the starting point. This is mainly because the drop of SNR when the target moves close to the cell edge of the allocated BSs. However, this problem can be solved by deploying multiple cooperative 5G BSs on the base of an ultra-dense network which can provide 40 – 50 BSs/km<sup>2</sup> [22].

### B. IMPACT OF ANTENNA NUMBER

Fig. 13 depicts the Root Mean Square Error (RMSE) of the speed and direction estimation results versus different  $M$ . It can be seen that both speed and direction estimations become more accurate with the increment of  $M$ . With more antennas equipped on the BS, we can harvest more signal components, which provides us a more accurate ACFS estimation. As a consequence, we can localize the peak more accurately and achieve better speed and direction estimations. When  $M \geq 150$ , further increasing the antenna number is not much helpful to improve the accuracy. This is reasonable because the ACFS estimation turns to be stable when  $M$  is large enough.

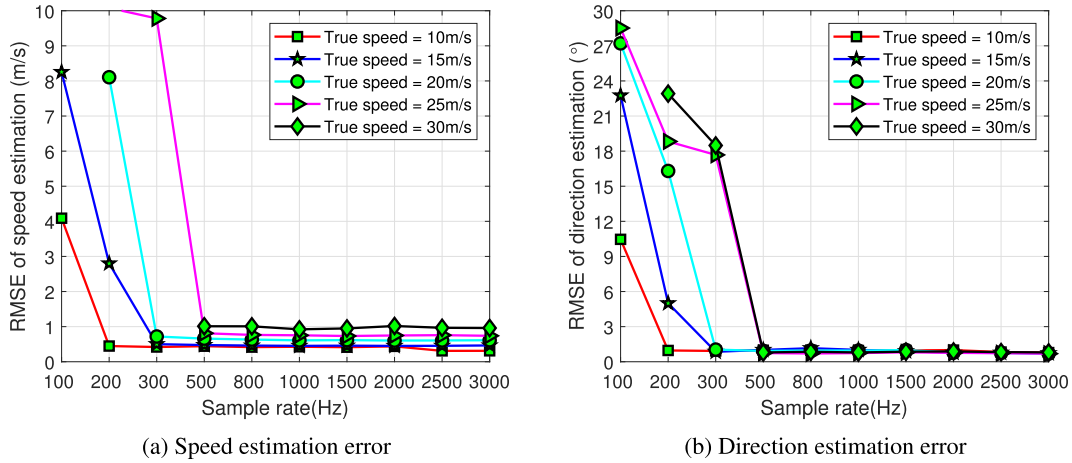
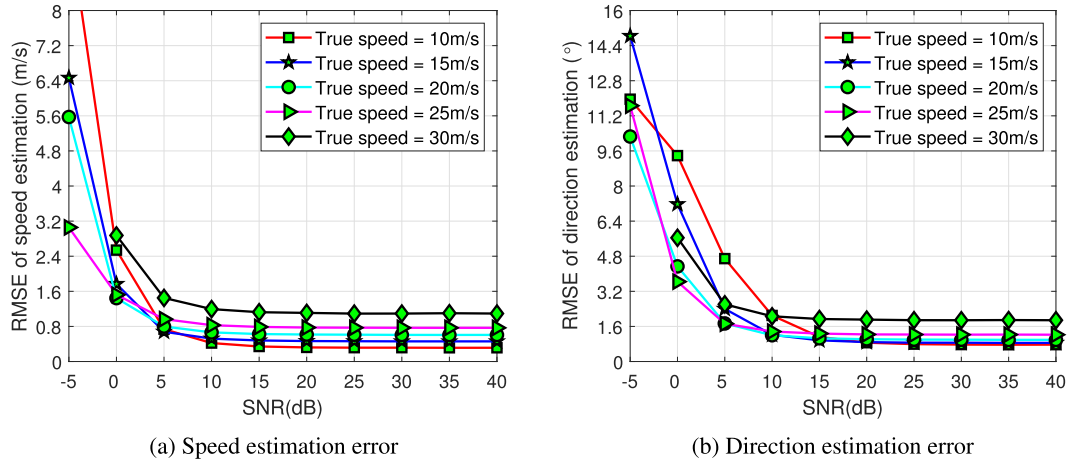
### C. IMPACT OF SAMPLE RATE

In general, a higher sample rate leads to a better accuracy. Given a specific sample rate, object moving at a higher speed tends to be more vulnerable. Assume the window length is

**FIGURE 11.** Speed and direction estimation results with variable speeds.**FIGURE 12.** CDF of estimation error.**FIGURE 13.** Estimation error versus antenna number.

$\Delta t$  during which the moving speed is constant. If the peak estimation is somehow deviated from the ground truth about one sample, then the velocity error is  $\Delta v = \frac{v}{f_s \Delta t}$ , indicating that a higher speed leads to a larger speed estimation error.

As a result, the corresponding direction estimation performance also degrades. Fig. 14 shows that the minimum sample rate for the proposed system is about 500Hz and further reducing the sample rate leads to larger estimation errors.

**FIGURE 14.** Estimation error versus sample rate.**FIGURE 15.** Estimation error versus SNR.

However, when the sample rate  $f_s \geq 500\text{Hz}$ , our system shows stable performance with a speed estimation error about  $0.9\text{m/s}$  and direction estimation error  $0.86^\circ$ . Since no other dedicated devices such as accelerometer and gyroscope are needed, it provides a promising candidate for moving speed and direction estimation in the future.

#### D. IMPACT OF SNR

Fig. 15 shows that the SNR threshold for our method to work well is  $10\text{dB}$ . If  $\text{SNR} \leq 10\text{dB}$ , both the speed and direction estimation performance degrade seriously. Fig. 15 also indicates that the estimation error increases when the target moves at a higher speed, which is consistent with our previous analysis.

#### E. IMPACT OF ANTENNA ARRAY CONFIGURATION

In this section, we study the impact of array configuration on our algorithm. In total, we consider three different array configurations including ULA, UCA and uniform rectangular array (URA) with  $M = 100$ ,  $H_B = 10\text{m}$  and  $L_{BR} \geq 50\text{m}$

(far-field scenario). Note that for the URA, the longer side consists of 41 antennas while there are 11 antennas on the shorter side because antennas on the four vertexes are shared by two adjacent sides of the rectangular array. Fig. 16 shows that all the three configurations achieve comparable performances. This is consistent with our analysis in Section III-B that different antenna array configurations show a similar focusing beam pattern in far-field scenario. As a result, our algorithm is independent on antenna configuration.

#### F. PERFORMANCE COMPARISON

First, we compare the speed estimation performance with the SenSpeed [29] and GPS based method [30]. Clearly, our algorithm shows better performance as shown in Fig. 17(a). Mainly, there are two reasons. First, SenSpeed relies on the assumption that the error between the integral value of acceleration and true speed increases almost linearly over time, which is not always true in practice. Second, GPS is vulnerable to urban canyon environments because of the NLOS distortions. Differently, our method uses the statistical

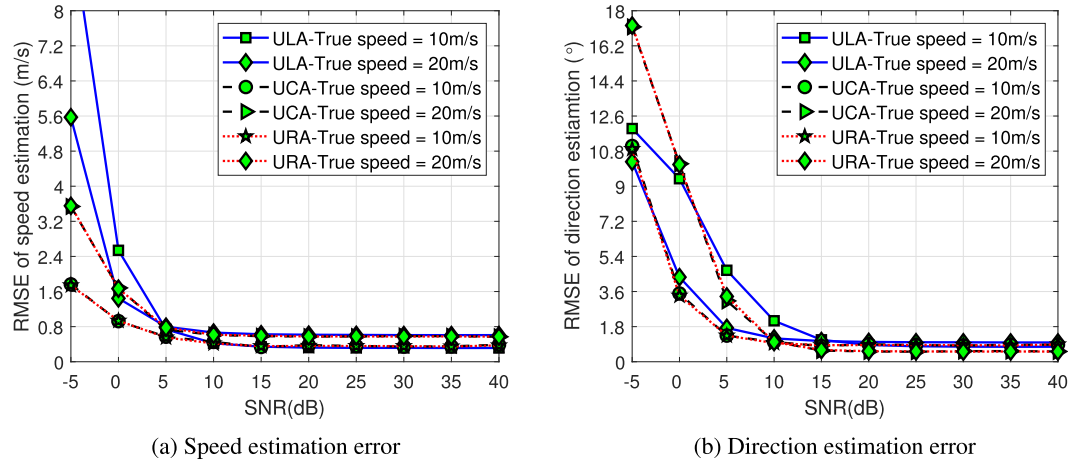


FIGURE 16. Estimation error versus different arrays (ULA, UCA and URA).

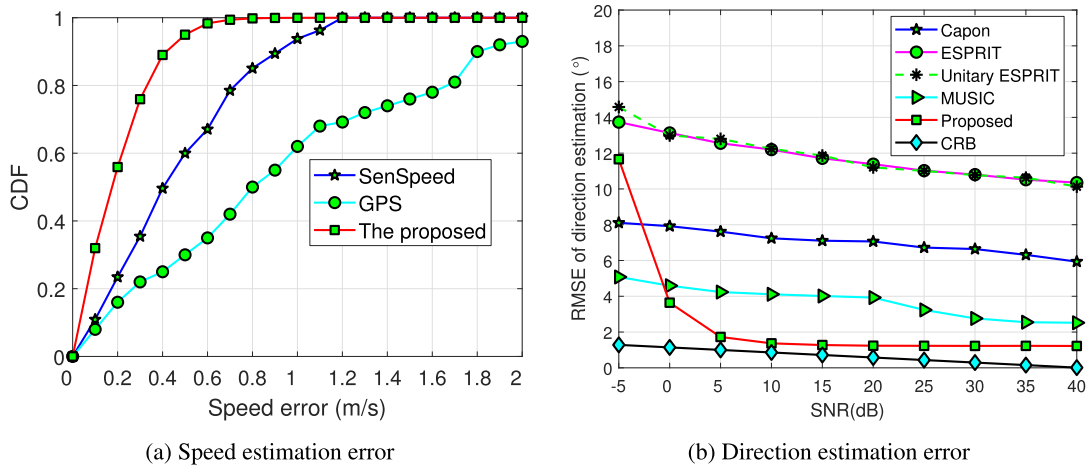


FIGURE 17. Performance comparison with related methods.

TABLE 1. Overall comparisons with existing works in RMSE.

Methods	Speed estimation Error (m/s)	Direction estimation error (°)	Complexity
INS [2], [3]	2-10 m/s	7-30	-
Massive MIMO [9], [12], [31]	0.8 - 3 m/s	0.1-5	$Mf_s + O(M^3)$
Vision based methods [5], [6]	1-5 m/s	0.2 - 6	-
Proposed ACFS method	$\leq 1.5$ m/s	$\leq 2$	$O(f_s)$

ACFS of the received signal to fully consider the NLOS signal components, which is more robust in real applications.

Fig. 17(b) compares the direction estimation performance of our method with four typical DOA estimation methods, i.e., Capon [25], MUSIC [26], ESPRIT [27] and Unitary ESPRIT [28]. In addition, Cramer-Rao Bound (CRB [36]) is also given to evaluate our method intuitively. Our method outperforms the DOA estimation methods mainly because that NLOS signal components are proved to have little impact on the ACFS of the received signal. However, most DOA

estimation methods require accurate time measurements of the LOS signal, which is very difficult to be extracted in the presence of NLOS signal components and noise in practice.

Table 1 compares our method with different moving speed and direction sensing schemes in both accuracy and complexity. Note that the complexity is based on the data collected in 1s. We do not show the complexity of INS and vision based methods because INS uses mechanical principle while the vision based methods rely on the image resolution.

As a result, their complexities are not only related to  $M$  and  $f_s$  but also other intrinsic factors.

Clearly, our method outperforms the INS system in accuracy. Although partial vision based algorithms show better performance in accuracy, they require dedicated camera to capture high resolution images and high computational power to process the graphs, thus hindering their practical applications. In addition, massive MIMO based DOA estimation methods deploy a large number of antennas on the receiver side to improve the angular resolution. Thus, the deployment cost and complexity increase rapidly with the increment of  $M$ . However, our method takes advantage of the existing massive antennas in 5G BS and uses only one received antenna on the receiver side to get a comparable performance. Overall, our method has two advantages. First, we do not need any dedicated devices but only one antenna on the receiver side. Second, the proposed method is independent on the environment and only needs to compute the statistical ACFS which greatly reduces the computation complexity and shows a great potential in real-time systems when 5G base station is available.

## VI. CONCLUSION

This paper proposes a novel RF signal-based moving speed and direction estimation method on the base of 5G massive MIMO communication system. We first prove that the ACFS of the received signal is highly related to the geometric shape of the antenna deployment in near-field scenario while it is a stationary sinc-like focusing beam in far-field scenario. A speed estimation algorithm is then explored based on the focusing beam. We further develop a novel moving direction estimation method by jointly using the location information of the nearby BSs in the ultra-dense 5G network. A massive MIMO system with carrier frequency about 28GHz is built to verify the proposed method. The impact of antenna number, sample rate, SNR and array configuration is also extensively studied. The results show that the proposed method can achieve about less than 1.5m/s speed estimation error and about less than 2° direction estimation error in different environments. The proposed RF based method does not require any dedicated device nor high computational power, it is an ideal candidate for future navigation applications.

## ACKNOWLEDGMENT

The authors sincerely thank the anonymous reviewers and the editors of IEEE Access for their helpful comments and constructive suggestions to improve this paper.

## REFERENCES

- [1] M. L. Thomas, "Evolution of GPS systems architecture and its impacts," *Commun. IIMA*, vol. 10, no. 4, p. 3, Jul. 2010.
- [2] Q. Fu, Y. Liu, Z. Liu, S. Li, and B. Guan, "Autonomous in-motion alignment for land vehicle strapdown inertial navigation system without the aid of external sensors," *J. Navigat.*, vol. 71, no. 6, pp. 1312–1328, Nov. 2018.
- [3] J. Jang, W.-G. Ahn, S. Seo, J. Lee, and J.-P. Park, "Flight test result for the ground-based radio navigation system sensor with an unmanned air vehicle," *Sensors*, vol. 15, no. 11, pp. 28472–28489, Nov. 2015.
- [4] P. Setoodeh, A. Khayatian, and E. Frajah, "Attitude estimation by separate-bias Kalman filter-based data fusion," *J. Navigat.*, vol. 57, no. 2, pp. 261–273, May 2004.
- [5] S. Naeem and S. Siraj, "A framework to select edge detection method using multi-criteria decision making," in *Proc. IEEE Int. Conf. Syst., Man, Cybern.*, Oct. 2013, pp. 730–735.
- [6] Z. Xian, X. He, J. Lian, X. Hu, and L. Zhang, "A bionic autonomous navigation system by using polarization navigation sensor and stereo camera," *Auton. Robots*, vol. 41, no. 5, pp. 1107–1118, Jun. 2017.
- [7] W. S. Gong, J. P. Chen, J. J. Lin, and H. Zhang, "The researches on vehicle-borne speed and direction detection method based on binocular image matching," in *Proc. IOP Conf. Mater. Sci. Eng.*, vol. 392, Aug. 2018, Art. no. 062116.
- [8] X. Zeng, M. Yang, B. Chen, and Y. Jin, "Estimation of direction of arrival by time reversal for low-angle targets," *IEEE Trans. Aerosp. Electron. Syst.*, vol. 54, no. 6, pp. 2675–2694, Dec. 2018.
- [9] D. Fan, F. Gao, G. Wang, Z. Zhong, and A. Nallanathan, "Angle domain signal processing-aided channel estimation for indoor 60-GHz TDD/FDD massive MIMO systems," *IEEE J. Sel. Areas Commun.*, vol. 35, no. 9, pp. 1948–1961, Sep. 2017.
- [10] A. Shahmansoori, G. E. Garcia, G. Destino, G. Seco-Granados, and H. Wyneersch, "Position and orientation estimation through millimeter-wave MIMO in 5G systems," *IEEE Trans. Wireless Commun.*, vol. 17, no. 3, pp. 1822–1835, Mar. 2018.
- [11] H. Huang, J. Yang, H. Huang, Y. Song, and G. Gui, "Deep learning for super-resolution channel estimation and DOA estimation based massive MIMO system," *IEEE Trans. Veh. Technol.*, vol. 67, no. 9, pp. 8549–8560, Sep. 2018.
- [12] N. Kassem, A. E. Kosba, and M. Youssef, "RF-based vehicle detection and speed estimation," in *Proc. IEEE 75th Veh. Technol. Conf. (VTC Spring)*, May 2012, pp. 1–5.
- [13] F. Zhang, C. Chen, B. Wang, H.-Q. Lai, and K. J. R. Liu, "A time-reversal spatial hardening effect for indoor speed estimation," in *Proc. IEEE Int. Conf. Acoust., Speech Signal Process. (ICASSP)*, Mar. 2017, pp. 5955–5959.
- [14] Z.-H. Wu, Y. Han, Y. Chen, and K. J. R. Liu, "A time-reversal paradigm for indoor positioning system," *IEEE Trans. Veh. Technol.*, vol. 64, no. 4, pp. 1331–1339, Apr. 2015.
- [15] F. Han, Y.-H. Yang, B. Wang, Y. Wu, and K. J. R. Liu, "Time-reversal division multiple access over multi-path channels," *IEEE Trans. Commun.*, vol. 60, no. 7, pp. 1953–1965, Jul. 2012.
- [16] Y. Chen, F. Han, Y.-H. Yang, H. Ma, Y. Han, C. Jiang, H.-Q. Lai, D. Claffey, Z. Safar, and K. J. R. Liu, "Time-reversal wireless paradigm for green Internet of Things: An overview," *IEEE Internet Things J.*, vol. 1, no. 1, pp. 81–98, Feb. 2014.
- [17] F. Zhang, C. Chen, B. Wang, H.-Q. Lai, Y. Han, and K. J. R. Liu, "WiBall: A Time-Reversal Focusing Ball Method for Decimeter-Accuracy Indoor Tracking," *IEEE Internet Things J.*, vol. 5, no. 5, pp. 4031–4041, Oct. 2018.
- [18] F. Zhang, C. Chen, B. Wang, and K. J. R. Liu, "WiSpeed: A statistical electromagnetic approach for device-free indoor speed estimation," *IEEE Internet Things J.*, vol. 5, no. 3, pp. 2163–2177, Jun. 2018.
- [19] Y. Azar, G. N. Wong, K. Wang, R. Mayzus, J. K. Schulz, H. Zhao, F. Gutierrez, D. Hwang, and T. S. Rappaport, "28 GHz propagation measurements for outdoor cellular communications using steerable beam antennas in New York city," in *Proc. IEEE Int. Conf. Commun. (ICC)*, Jun. 2013, pp. 5143–5147.
- [20] E. Ben-Dor, T. S. Rappaport, Y. Qiao, and S. J. Lauffenburger, "Millimeter-wave 60 GHz outdoor and vehicle AOA propagation measurements using a broadband channel sounder," in *Proc. IEEE Global Telecommun. Conf. (GLOBECOM)*, Dec. 2011, pp. 1–6.
- [21] A. I. Sulyman, A. T. Nassar, M. K. Samimi, G. R. Maccartney, T. S. Rappaport, and A. Alsanie, "Radio propagation path loss models for 5G cellular networks in the 28 GHZ and 38 GHZ millimeter-wave bands," *IEEE Commun. Mag.*, vol. 52, no. 9, pp. 78–86, Sep. 2014.
- [22] X. Ge, S. Tu, G. Mao, and C. X. Wang, "5G ultra-dense cellular networks," *IEEE Trans. Wireless Commun.*, vol. 23, no. 1, pp. 72–79, Feb. 2016.
- [23] C.-X. Wang, F. Haider, X. Gao, X.-H. You, Y. Yang, D. Yuan, H. Aggoune, H. Haas, S. Fletcher, and E. Hepsaydir, "Cellular architecture and key technologies for 5G wireless communication networks," *IEEE Commun. Mag.*, vol. 52, no. 2, pp. 122–130, Feb. 2014.

- [24] O. Galinina, A. Pyatyaev, S. Andreev, M. Dohler, and Y. Koucheryavy, "5G multi-RAT LTE-WiFi ultra-dense small cells: Performance dynamics, architecture, and trends," *IEEE J. Sel. Areas Commun.*, vol. 33, no. 6, pp. 1224–1240, Jun. 2015.
- [25] J. Li, P. Stoica, and Z. Wang, "On robust capon beamforming and diagonal loading," *IEEE Trans. Signal Process.*, vol. 51, no. 7, pp. 1702–1715, Jul. 2003.
- [26] R. Schmidt, "Multiple emitter location and signal parameter estimation," *IEEE Trans. Antennas Propag.*, vol. 34, no. 3, pp. 276–280, Mar. 1986.
- [27] R. Roy and T. Kailath, "ESPRIT-estimation of signal parameters via rotational invariance techniques," *IEEE Trans. Acoust., Speech, Signal Process.*, vol. 37, no. 7, pp. 984–995, Jul. 1989.
- [28] M. Haardt and J. Nossek, "Unitary ESPRIT: How to obtain increased estimation accuracy with a reduced computational burden," *IEEE Trans. Signal Process.*, vol. 43, no. 5, pp. 1232–1242, May 1995.
- [29] J. Yu, H. Zhu, H. Han, Y. J. Chen, J. Yang, Y. Zhu, Z. Chen, G. Xue, and M. Li, "SenSpeed: Sensing driving conditions to estimate vehicle speed in urban environments," *IEEE Trans. Mobile Comput.*, vol. 15, no. 1, pp. 202–216, Jan. 2016.
- [30] A. Gorski, "Understanding GPS performance in urban environments," *Tech. Rep.*, 2011. [Online]. Available: <http://blogs.agi.com/agi/2011/01/04/understanding-gps-performance-in-urban-environments/>
- [31] C. Xu, L. Daniel, E. Hoare, V. Sizov, and M. Cherniakov, "Comparison of speed over ground estimation using acoustic and radar Doppler sensors," in *Proc. 2014 11th Eur. Radar Conf.*, Oct. 2014, pp. 189–192.
- [32] L. Borcea, G. Papanicolaou, and C. Tsogka, "Theory and applications of time reversal and interferometric imaging," *Inverse Problems*, vol. 19, no. 6, pp. S139–S164, Dec. 2003.
- [33] C. Xiao, Y. Zheng, and N. Beaulieu, "Novel sum-of-sinusoids simulation models for Rayleigh and Rician fading channels," *IEEE Trans. Wireless Commun.*, vol. 5, no. 12, pp. 3667–3679, Dec. 2006.
- [34] R. Muller, D. A. Dupleich, C. Schneider, R. Herrmann, and R. S. Thoma, "Ultrawideband 3D mmWave channel sounding for 5G," in *Proc. XXXIth URSI Gen. Assem. Sci. Symp. (URSI GASS)*, Aug. 2014, pp. 1–4.
- [35] W. S. Cleveland, "Robust locally weighted regression and smoothing scatterplots," *J. Amer. Stat. Assoc.*, vol. 74, no. 368, pp. 829–836, Dec. 1979.
- [36] P. Stoica and A. Nehorai, "MUSIC, maximum likelihood, and Cramer-Rao bound," *IEEE Trans. Acoust., Speech, Signal Process.*, vol. 37, no. 5, pp. 720–741, May 1989.



**FENG ZHANG** (Member, IEEE) received the B.S. and M.S. degrees from the Department of Electronic Engineering and Information Science, University of Science and Technology of China, Hefei, in 2011 and 2014, respectively, and the Ph.D. degree from the Department of Electrical and Computer Engineering, University of Maryland, College Park, MA, USA, in December 2018. He is currently with Origin Wireless, Inc. His research interests include wireless sensing, statistical signal processing, and wireless indoor localization. He was a recipient of the Distinguished TA Award from the University of Maryland and the State Scholarship from the University of Science and Technology of China.



**BEIBEI WANG** (Senior Member, IEEE) received the B.S. degree (Hons.) in electrical engineering from the University of Science and Technology of China, Hefei, in 2004, and the Ph.D. degree in electrical engineering from the University of Maryland, College Park, MA, USA, in 2009. She was with the University of Maryland as a Research Associate, from 2009 to 2010, and with Qualcomm Research and Development, from 2010 to 2014. Since 2015, she has been with Origin Wireless Inc., where she is currently a Chief Scientist. Her research interests include wireless sensing, positioning, machine learning, communications, and signal processing. She received the Graduate School Fellowship, the Future Faculty Fellowship, and the Dean's Doctoral Research Award from the University of Maryland, and the Overview Paper Award from the IEEE Signal Processing Society, in 2015. She is a coauthor of the *Cognitive Radio Networking and Security: A Game-Theoretic View* (Cambridge University Press, 2010) and the *Wireless AI: Wireless Sensing, Positioning, IoT, and Communications* (Cambridge University Press, 2019).



**K. J. RAY LIU** (Fellow, IEEE) is currently a Distinguished University Professor and a Distinguished Scholar-Teach of University of Maryland, College Park, MA, USA, where he is also the Christine Kim Eminent Professor of information technology. He leads the Maryland Signals and Information Group, conducting research encompassing broad areas of information and communications technology, with the recent focus on wireless AI for indoor tracking and wireless sensing.

Dr. Liu was the IEEE Vice President, Technical Activities, and a member of the IEEE Board of Director as the Division IX Director. He has served as the President of the IEEE Signal Processing Society, where he was the Vice President - Publications and Board of Governor. He was a recipient of the 2016 IEEE Leon Kirchmayer Award on graduate teaching and mentoring, the IEEE Signal Processing Society 2014 Society Award, the IEEE Signal Processing Society 2009 Technical Achievement Award, and over a dozen of best paper awards. He is recognized by Web of Science as a Highly Cited Researcher. As the founder of Origin Wireless, his invention won the 2017 CEATEC Grand Prix Award and CES 2020 Innovation Award. He is a Fellow of the AAAS and National Academy of Inventors. He also received teaching and research recognitions from University of Maryland, including university-level Invention of the Year Award; and college-level Poole and Kent Senior Faculty Teaching Award, Outstanding Faculty Research Award, and Outstanding Faculty Service Award, all from A. James Clark School of Engineering. He has also served as the Editor-in-Chief of the *IEEE Signal Processing Magazine*.



**XIAOLU ZENG** received the B.S. degree from the Harbin Institute of Technology ( HIT ), China, in 2014. He is currently pursuing the Ph.D. degree with the School of Electronic Engineering, Xidian University, China. Since September 2017, he has been a visiting student at the Department of Electrical and Computer Engineering, University of Maryland at College Park, College Park, MD, USA, with the support of the China Scholarship Council ( CSC ). His current research interests include array signal processing, multipath exploration using time reversal technique, parameter estimation, and time reversal based wireless communication, target detection, as well as localization, tracking, and classification.